

RESEARCH ARTICLE

[View Article Online](#)
[View Journal](#) | [View Issue](#)



Cite this: *Inorg. Chem. Front.*, 2023, **10**, 2014

Received 29th December 2022,
Accepted 13th February 2023

DOI: 10.1039/d2qi02757g
rsc.li/frontiers-inorganic

Rare-earth La-doped VS_{2-x} for electrochemical nitrate reduction to ammonia†

Guohui Wang,‡^a Peng Shen,‡^a Kai Chen,^a Yali Guo,^a Xiaolin Zhao^b and Ke Chu ^a

We report rare-earth La-doped VS_{2-x} enriched with S-vacancies (La- VS_{2-x}) towards the electrochemical nitrate reduction to ammonia (NO_3RR), which shows a maximum NH_3 -faradaic efficiency of 96.6% with a corresponding NH_3 yield rate of $11.3\text{ mg h}^{-1}\text{ cm}^{-2}$ at -0.6 V vs. RHE. Theoretical computations unveil that La-dopants and S-vacancies synergistically promote NO_3^- activation, suppress hydrogen evolution and lower the energetic barriers, leading to the enhanced NO_3RR activity and selectivity of La- VS_{2-x} .

1. Introduction

NH_3 , a value-added chemical and also a renewable hydrogen-rich carrier, is vital to modern agriculture and industry.^{1–3} Electrochemical nitrate reduction to ammonia (NO_3RR) represents a fascinating approach to realising both green NH_3 generation and wastewater purification.^{4–6} However, NO_3RR effectiveness is still retarded by the complex multi-electron transfer process and easy occurrence of side reactions especially competing for the hydrogen evolution reaction (HER).^{7–9} Therefore, it is urgently required to explore effective NO_3RR electrocatalysts for active and selective NO_3^- -to- NH_3 conversion.^{10–14}

To date, substantial efforts have been devoted to exploring many potential NO_3RR catalysts.^{15–25} Metal chalcogenides have attracted wide attention in electrolysis due to their layered structure and high electrochemical stability.^{26–28} Among them, VS_2 is most appealing due to its metallic nature with high conductivity, facilitating accelerated electron transfer for boosting the catalytic kinetics.^{29,30} Nevertheless, investigations on VS_2 -based catalysts for the NO_3RR remain largely unexplored due presumably to the poor intrinsic activity of VS_2 for NO_3^- activation. Metal doping is a promis-

ing approach to tuning the surface electronic structure of the catalysts to significantly enhance the catalytic activity.³¹ By virtue of the unique 4f structure and rich redox capability, rare-earth lanthanides emerge as intriguing metal dopants to considerably improve the catalyst activities.^{32–34} Nevertheless, the use of rare-earth metal dopants to tune the electronic structure and NO_3RR activity of the catalysts has not yet been explored.

In this study, we report a rare-earth La-doped VS_{2-x} (La- VS_{2-x}) enriched with S-vacancies (V_s) towards the NO_3RR . La- VS_{2-x} delivers excellent NO_3RR performance with a highest NH_3 -faradaic efficiency (FE_{NH_3}) of 96.6% with the corresponding NH_3 yield of $11.3\text{ mg h}^{-1}\text{ cm}^{-2}$ at -0.6 V vs. RHE. Detailed experiments combined with theoretical investigations are employed to unravel the catalytic NO_3RR mechanism of La- VS_{2-x} .

2. Results and discussion

La- VS_{2-x} (4.8 wt% La) grown on carbon cloth (CC) was fabricated using a simple hydrothermal approach. The XRD pattern of La- VS_{2-x} (Fig. 1a) shows major diffraction peaks assigned to the hexagonal VS_2 phase (JCPDS No. 89-1640). The SEM image of La- VS_{2-x} (Fig. 1b) shows numerous nanosheets which grow perpendicularly on the CC substrate, and the nanosheet morphology of La- VS_{2-x} is further verified by the TEM image (Fig. 1c). The elemental mapping images of La- VS_{2-x} (Fig. 1d) reveal a uniform distribution of La elements. The HRTEM image of La- VS_{2-x} (Fig. 1e) shows two d spacings of 0.25 and 0.60 nm, corresponding to the (011) and (001) facets of VS_2 , respectively. The corresponding

^aSchool of Materials Science and Engineering, Lanzhou Jiaotong University, Lanzhou 730070, China. E-mail: chuk630@mail.lzjtu.cn

^bNational Engineering Laboratory for Electric Vehicles, Beijing Institute of Technology, Beijing 100081, Beijing, China

† Electronic supplementary information (ESI) available. See DOI: <https://doi.org/10.1039/d2qi02757g>

‡These authors contributed equally to this work.

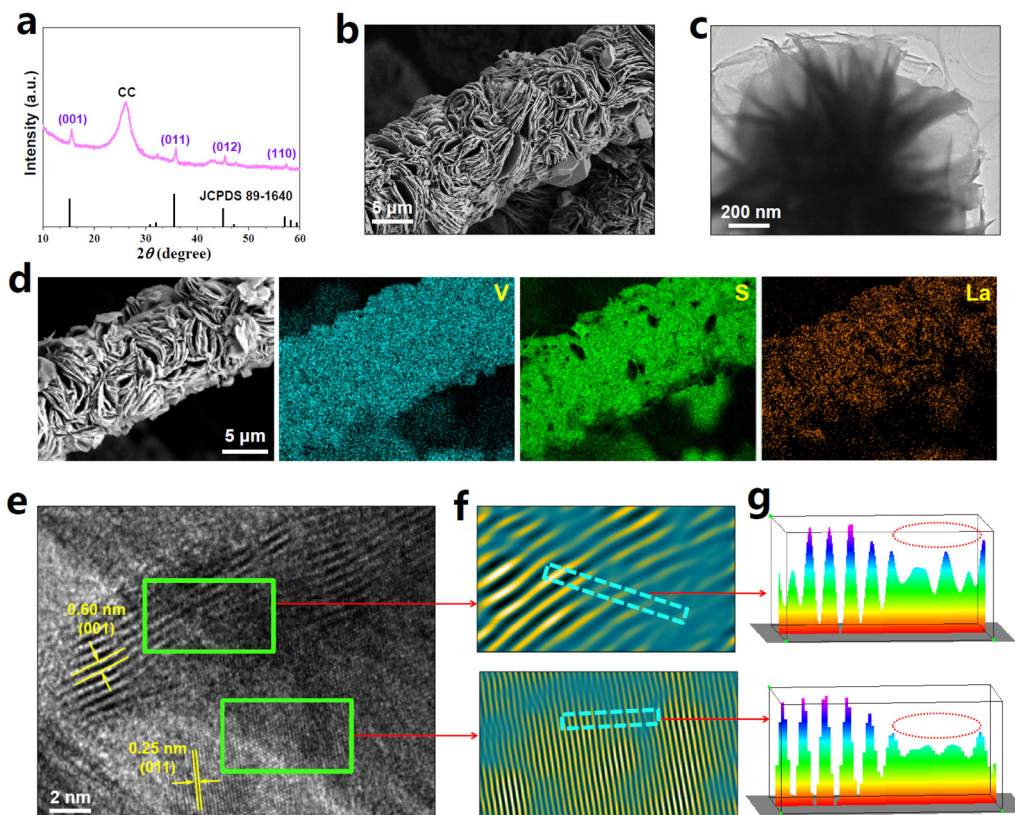


Fig. 1 (a) XRD pattern of La-VS_{2-x} on CC. (b) SEM image of La-VS_{2-x} on CC. (c) TEM image of La-VS_{2-x}. (d) Elemental mapping images of La-VS_{2-x} on CC. (e) HRTEM image of La-VS_{2-x} and (f) the corresponding IFFT pattern and (g) lattice line scanning analyses.

inverse fast Fourier transform (IFFT) pattern (Fig. 1f) and lattice line scanning analysis (Fig. 1g) signify the loss of some lattice atoms (dotted circles), indicating the presence of abundant defects/vacancies on La-VS_{2-x}.³⁵ The elemental analysis further reveals a much reduced S/V molar ratio of 1.85 compared to the nominal ratio of VS₂ (2), demonstrating the V_S-rich nature of La-VS_{2-x}.³⁶

As shown in the electron paramagnetic resonance (EPR) spectrum (Fig. 2a), La-VS_{2-x} displays a much enhanced EPR signal compared to pristine VS₂, further attesting to the existence of abundant V_S on La-VS_{2-x}.³⁶⁻³⁹ The X-ray absorption near-edge structure (XANES) spectra (Fig. 2b) show that the white line intensity of La-VS_{2-x} is lower than that of the La₂O₃ reference, suggesting that La-dopants carry a partially positive charge.⁴⁰ The extended X-ray absorption fine structure (EXAFS) spectra (Fig. 2c) show that La-VS_{2-x} presents a dominant peak at 2.16 Å, assigned to the La-S scattering path. Besides, no La-La (3.96 Å) scattering paths can be detected, confirming that La-dopants are atomically dispersed in La-VS_{2-x}. The evidence for the presence of atomically dispersed La-dopants in La-VS_{2-x} can be further proved by the wavelet transform (WT) plots (Fig. 2d), showing the absence of a La-La signal in La-VS_{2-x}.⁴¹⁻⁴³ The EXAFS fitting results (Fig. 2e, Table S1†) reveal that the La-S coordination is around 5, implying that La-

dopants mainly substitute the five-fold coordinated V atoms of VS_{2-x} (Fig. 2f).

Theoretical calculations are carried out to examine the electronic structure of La-VS_{2-x}. The calculated La-dopant formation energy (E_{La} , Fig. S1†) reveals a much reduced E_{La} of La-VS_{2-x} (1.94 eV) compared to V_S-free La-VS₂ (3.61 eV), suggesting that V_S plays a critical role in making the incorporation of La-dopants into VS_{2-x} lattices more thermodynamically feasible.^{43,44} Electron contour maps reveal abundant electrons accumulated in the V_S region (Fig. S2 and S3†), while La-dopant affects little the electron accumulation nature of V_S in La-VS_{2-x} (Fig. 2g). These accumulated electrons are apt to be transferred to the antibonding orbital of NO₃⁻ for the activation and dissociation of the N=O bond,^{5,45} facilitating the boosted NO₃RR process. The partial densities of states (PDOS) plot of La-VS_{2-x} (Fig. S4†) reveals a significant La/S orbital hybridization, suggesting the strong La-S electronic interactions which allow La-dopants to be atomically dispersed and firmly stabilized in VS_{2-x}, resulting in the high thermodynamic stability of La-VS_{2-x} (Fig. S5†).⁴⁶ Furthermore, compared to VS₂ and VS_{2-x}, La-dopant incorporation makes La-VS_{2-x} exhibit the occupied electron states across the Fermi level (Fig. 2h) and reduced work function (Fig. S6†), thus endowing La-VS_{2-x} with enhanced conduc-

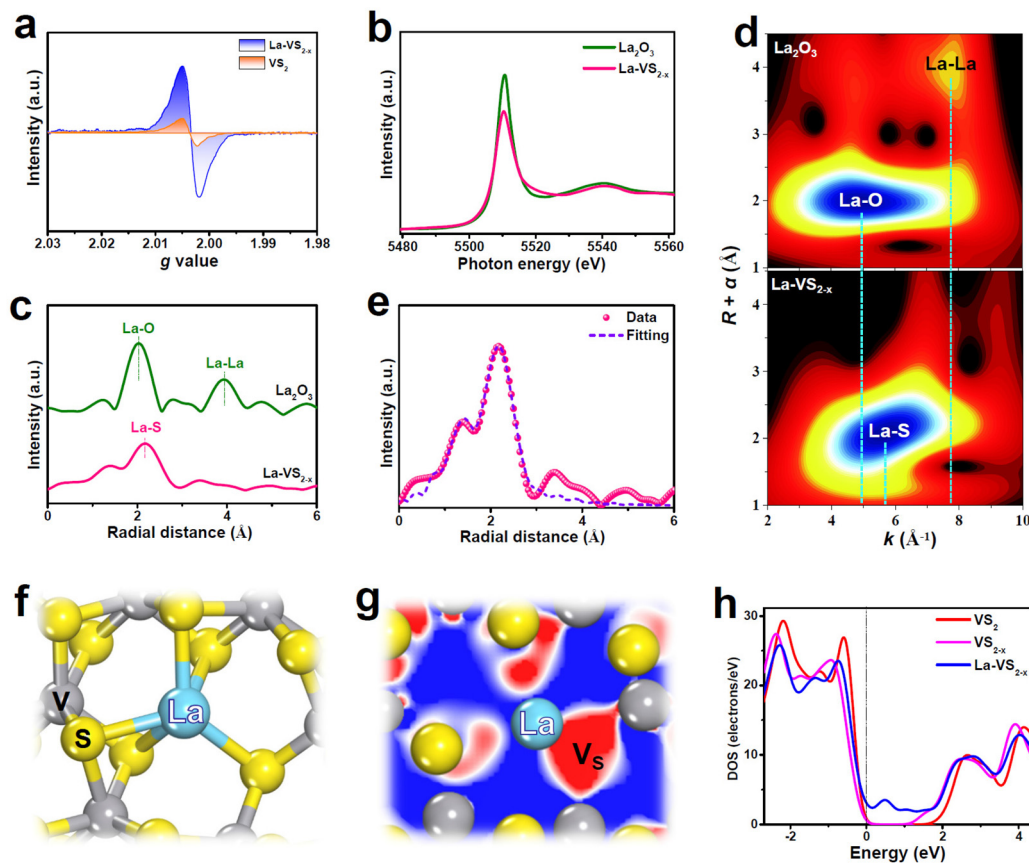


Fig. 2 (a) EPR spectra of VS_2 and La-VS_{2-x} . (b) La L_3 -edge XANES, (c) EXAFS spectra and (d) WT profiles of La-VS_{2-x} and reference La_2O_3 . (e) EXAFS fitting curve of La-VS_{2-x} and (f) the corresponding fitting model. (g) Electron contour map of La-VS_{2-x} (red: charge accumulation, blue: charge depletion). (h) DOS plots of VS_2 , VS_{2-x} and La-VS_{2-x} .

tivity to accelerate electron transfer and catalytic kinetics (Fig. S7†).^{47–51}

The electrochemical NO_3RR activity of La-VS_{2-x} directly used as the working electrode is evaluated in an H-type cell on the basis of a standard procedure flow chart (Fig. S8†).^{52–55} The electrolyte used is 0.5 M Na_2SO_4 with 0.1 M NaNO_3 (Fig. S9†). As displayed in Fig. 3a, La-VS_{2-x} exhibits a much higher current density in the presence of NO_3^- , indicating that La-VS_{2-x} is catalytically effective towards the NO_3RR . The NH_3 yield rates and FE_{NH_3} of La-VS_{2-x} are then quantitatively estimated by the combination of chronoamperometric (Fig. S10†) and colorimetric approaches (Fig. S11–S13†).^{56–59} As shown in Fig. 3b, La-VS_{2-x} exhibits the highest FE_{NH_3} of 96.6% at -0.6 V. The corresponding NH_3 yield rate and partial current density at -0.6 V are 11.3 $\text{mg h}^{-1} \text{cm}^{-2}$ and 121.2 mA cm^{-2} (Fig. S14†), respectively. Such NO_3RR performance of La-VS_{2-x} exceeds that of most reported NO_3RR catalysts (Fig. 3c, Table S2†). We also investigate the effect of the La-dopant content on the NO_3RR performance of La-VS_{2-x} and determine that 4.8 wt% is the optimum La-dopant content (Fig. S15†). Meanwhile, FE_{NH_3} is dramatically higher than the FEs of other byproducts shown in Fig. 3d,

demonstrating the exceptional selectivity of La-VS_{2-x} for electrocatalytic NO_3^- -to- NH_3 conversion.

Several control tests are carried out to validate the NH_3 origin. It is shown in Fig. S16† that NH_3 is barely detected both in the NO_3^- -free electrolyte and at the open circuit potential (OCP). The N source is further confirmed by isotopic labeling ^1H nuclear magnetic resonance (NMR) spectroscopy (Fig. 3e). Visibly, upon using $^{14}\text{NO}_3^-$ and $^{15}\text{NO}_3^-$ tracing agents, the resulting NMR spectra show three characteristic signals of $^{14}\text{NH}_4^+$ and two signals of $^{15}\text{NH}_4^+$, respectively, proving that the detected NH_3 originates from the NO_3RR .^{60–62} We further tested the catalytic stability of La-VS_{2-x} for the NO_3RR . Fig. 3f depicts no obvious decay in NH_3 yield rates and FE_{NH_3} during ten consecutive NO_3RR cycles, indicating the good cycling durability of La-VS_{2-x} . During the chronopotentiometric test for 20 h of continuous electrolysis (Fig. 3g), negligible variations in current density and corresponding FE_{NH_3} can be observed, suggesting the outstanding long-term stability of La-VS_{2-x} . After the stability tests, La-VS_{2-x} reveals no obvious changes in the morphology, crystal phase and La content (Fig. S17†), confirming the robust structural and compositional stability of La-VS_{2-x} .

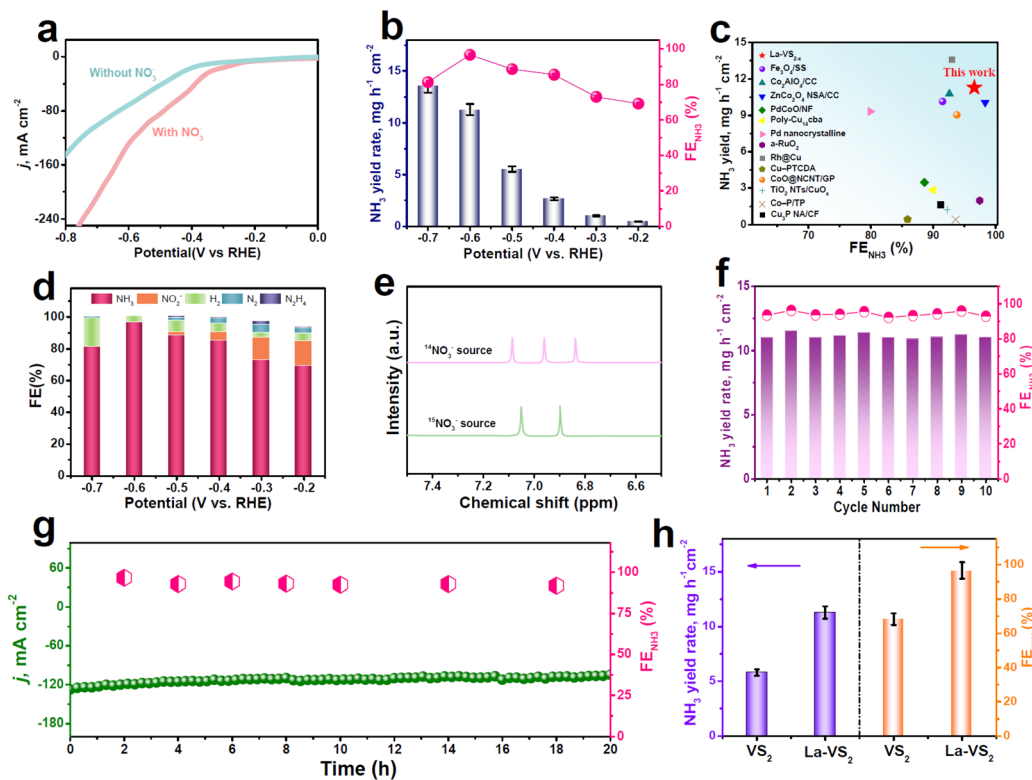


Fig. 3 (a) LSV curves of La-VS_{2-x} with and without the addition of 0.1 M NO_3^- . (b) NH_3 yield rates and FE_{NH_3} of La-VS_{2-x} at various potentials. (c) NO_3RR performance comparison between La-VS_{2-x} and reported catalysts. (d) FEs of different products after NO_3RR electrolysis at various potentials. (e) ¹H NMR measurements fed by ¹⁴NO₃⁻/¹⁵NO₃⁻ after NO_3RR electrolysis. (f) Cycling and (g) long-term chronoamperometry tests at -0.6 V. (h) Comparison of the NO_3RR performance between VS₂ and La-VS_{2-x} at -0.6 V.

We also evaluate the NO_3RR activity of pristine VS₂ under the same conditions at -0.6 V (Fig. 3h). Obviously, the NO_3RR performance of VS_{2-x} is considerably lower than that of La-VS_{2-x}, with FE_{NH_3} and the corresponding NH_3 yield rate being 1.4 and 1.9 times poorer than those of La-VS_{2-x}, respectively, suggesting that La-dopants have a significant contribution to the NO_3RR activity of La-VS_{2-x}. We measured the electrochemical surface areas (ECSAs) of the two catalysts and found that the ECSA-normalized performance of La-VS_{2-x} is still considerably better than that of VS₂ (Fig. S18†), indicating the superior intrinsic NO_3RR activity of La-VS_{2-x}. The in-depth mechanistic understanding of the enhanced NO_3RR of La-VS_{2-x} is elucidated by theoretical investigations.

Since NO_3^- adsorption is a critical prerequisite for the NO_3RR ,⁶³ we first examined NO_3^- adsorption on various catalysts. As shown in Fig. S19,† in contrast to the negligible N=O bond elongation on pristine VS₂, the N=O bond of the adsorbed NO_3^- on the V_S site of VS_{2-x} is stretched to 1.305 Å, and it is further stretched to 1.365 Å on La-dopant-adjacent V_S site of La-VS_{2-x}, indicating that NO_3^- can be significantly activated on La-VS_{2-x}. This is further corroborated by the differential charge density maps, showing that compared to the cases of VS₂ and VS_{2-x} (Fig. S20†), La-VS_{2-x} exhibits a more intense charge transfer with the adsorbed NO_3^- (Fig. 4a). The corresponding electron location function maps (Fig. 4b) reveal that

both the V_S-induced unsaturated V atom and the La-dopant (or La-V_S site) synergistically donate electrons to the adsorbed NO_3^- ,³⁵ resulting in effective NO_3^- activation on La-VS_{2-x}. Benefiting from the enhanced NO_3^- activation on the La-V_S site, La-VS_{2-x} shows a largely reduced binding free energy of NO_3^- relative to VS₂ and VS_{2-x} (Fig. 4c), thus facilitating the subsequent NO_3RR process. Meanwhile, compared to the V_S site of VS_{2-x}, the La-V_S site of La-VS_{2-x} exhibits a more energy requirement for H₂ evolution (Fig. 4d), and thus La-VS_{2-x} can effectively impede the HER to benefit NO_3RR selectivity.⁵⁶

The free energy changes of NO_3RR pathways of all considered VS₂, VS_{2-x} and La-VS_{2-x} catalysts are further assessed, with their corresponding atom configurations being displayed in Fig. S21–S23.† It is known that the electrocatalytic NO_3RR process for NH₃ formation comprises the initial deoxidation steps of * NO_3 → * NO_2 → * NO and the following hydrogenation steps of * NOH → * N → * NH → * NH_2 → * NH_3 .^{64–66} As shown in Fig. 4e, in comparison with VS₂ and VS_{2-x}, La-VS_{2-x} shows the lowest energy barrier of -0.63 eV for its rate-determining step (RDS) of * NO → * NOH , suggesting its favorable energetics to boost the NO_3RR process. Therefore, the co-introduction of V_S and La-dopants can synergistically promote NO_3^- activation, retard the HER and lower the reaction energetic barriers, thereby greatly promoting the NO_3RR activity and selectivity of La-VS_{2-x} for NO_3^- -to-NH₃ conversion.

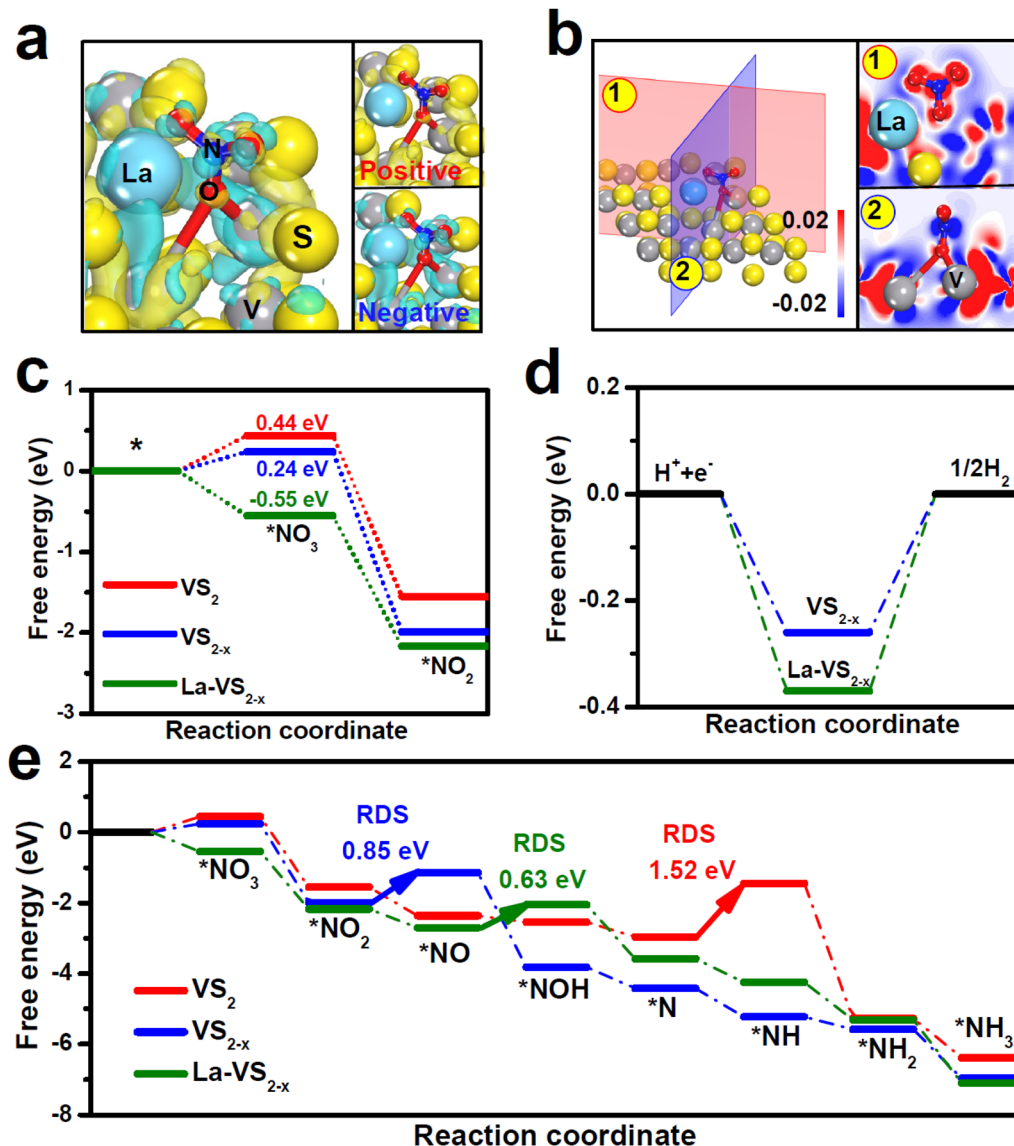


Fig. 4 (a) Differential charge density maps of NO₃⁻ adsorption on La-VS_{2-x} (yellow: accumulation, cyan: depletion) and (b) the corresponding electron location function maps (red: accumulation, blue: depletion). (c and d) Binding free energies of (c) NO₃⁻ and (d) H on different catalysts. (e) Gibbs free energy diagrams of the NO₃RR pathway of VS₂, VS_{2-x} and La-VS_{2-x}, respectively.

3. Conclusion

In summary, La-VS_{2-x} is verified to be a highly active and selective NO₃RR catalyst. Theoretical computations reveal that the excellent NO₃RR performance of La-VS_{2-x} originates from the synergy of La-dopants and V_S to promote NO₃⁻ activation, suppress the HER and lower the energetic barriers. This work demonstrates the great potential of rare earth catalysts toward the efficient NO₃RR for NH₃ electrosynthesis.

Conflicts of interest

There are no conflicts of interest to declare.

Acknowledgements

This work was supported by the Central Government Guides Local Science and Technology Development Project (206Z1003G) and the Longyuan Youth Innovative and Entrepreneurial Talents Project ([2021]17).

References

- 1 J. Liang, Q. Liu, A. A. Alshehri and X. Sun, Recent advances in nanostructured heterogeneous catalysts for N-cycle electrocatalysis, *Nano Res. Energy*, 2022, **1**, e9120010.

2 K. Chen, P. Shen, N. Zhang, D. Ma and K. Chu, Electrocatalytic NO reduction to NH₃ on Mo₂C nanosheets, *Inorg. Chem.*, 2023, **62**, 653–658.

3 D. Qi, F. Lv, T. Wei, M. Jin, G. Meng, S. Zhang, Q. Liu, W. Liu, D. Ma, M. S. Hamdy, J. Luo and X. Liu, High-efficiency electrocatalytic NO reduction to NH₃ by nanoporous VN, *Nano Res. Energy*, 2022, **1**, e9120022.

4 H. Xu, Y. Ma, J. Chen, W.-x. Zhang and J. Yang, Electrocatalytic reduction of nitrate—a step towards a sustainable nitrogen cycle, *Chem. Soc. Rev.*, 2022, **51**, 2710–2758.

5 Y. Wang, C. Wang, M. Li, Y. Yu and B. Zhang, Nitrate electroreduction: mechanism insight, in situ characterization, performance evaluation, and challenges, *Chem. Soc. Rev.*, 2021, **50**, 6720–6733.

6 P. H. van Langevelde, I. Katsounaros and M. T. Koper, Electrocatalytic nitrate reduction for sustainable ammonia production, *Joule*, 2021, **5**, 290–294.

7 N. Zhang, J. Shang, X. Deng, L. Cai, R. Long, Y. Xiong and Y. Chai, Governing interlayer strain in bismuth nanocrystals for efficient ammonia electrosynthesis from nitrate reduction, *ACS Nano*, 2022, **16**, 4795–4804.

8 Y. Wang, H. Li, W. Zhou, X. Zhang, B. Zhang and Y. Yu, Structurally disordered RuO₂ nanosheets with rich oxygen vacancies for enhanced nitrate electroreduction to ammonia, *Angew. Chem.*, 2022, **134**, e202202604.

9 H. Liu, X. Lang, C. Zhu, J. Timoshenko, M. Rüscher, L. Bai, N. Guijarro, H. Yin, Y. Peng, J. Li, W. Wang, B. Roldan Cuenya and J. Luo, Efficient electrochemical nitrate reduction to ammonia with copper-supported rhodium cluster and single-atom catalysts, *Angew. Chem.*, 2022, **134**, e202202556.

10 Q. Gao, H. S. Pillai, Y. Huang, S. Liu, Q. Mu, X. Han, Z. Yan, H. Zhou, Q. He, H. Xin and H. Zhu, Breaking adsorption-energy scaling limitations of electrocatalytic nitrate reduction on intermetallic CuPd nanocubes by machine-learned insights, *Nat. Commun.*, 2022, **13**, 2338.

11 X. F. Cheng, J. H. He, H. Q. Ji, H. Y. Zhang, Q. Cao, W. J. Sun, C. L. Yan and J. M. Lu, Coordination symmetry breaking of single-atom catalysts for robust and efficient nitrate electroreduction to ammonia, *Adv. Mater.*, 2022, **34**, 2205767.

12 F.-Y. Chen, Z.-Y. Wu, S. Gupta, D. J. Rivera, S. V. Lambeets, S. Pecaut, J. Y. T. Kim, P. Zhu, Y. Z. Finfrock, D. M. Meira, G. King, G. Gao, W. Xu, D. A. Cullen, H. Zhou, Y. Han, D. E. Perea, C. L. Muhich and H. Wang, Efficient conversion of low-concentration nitrate sources into ammonia on a Ru-dispersed Cu nanowire electrocatalyst, *Nat. Nanotechnol.*, 2022, **17**, 759–767.

13 Z. Deng, C. Ma, Z. Li, Y. Luo, L. Zhang, S. Sun, Q. Liu, J. Du, Q. Lu, B. Zheng and X. Sun, High-efficiency electrochemical nitrate reduction to ammonia on a Co₃O₄ nanoarray catalyst with cobalt vacancies, *ACS Appl. Mater. Interfaces*, 2022, **14**, 46595–46602.

14 Z. Deng, C. Ma, X. Fan, Z. Li, Y. Luo, S. Sun, D. Zheng, Q. Liu, J. Du, Q. Lu, B. Zheng and X. Sun, Construction of CoP/TiO₂ nanoarray for enhanced electrochemical nitrate reduction to ammonia, *Mater. Today Phys.*, 2022, **28**, 100854.

15 Y. Xu, Y. Wen, T. Ren, H. Yu, K. Deng, Z. Wang, X. Li, L. Wang and H. Wang, Engineering the surface chemical microenvironment over CuO nanowire arrays by polyaniline modification for efficient ammonia electrosynthesis from nitrate, *Appl. Catal., B*, 2023, **320**, 121981.

16 Y. Xu, Y. Sheng, M. Wang, T. Ren, K. Shi, Z. Wang, X. Li, L. Wang and H. Wang, Interface coupling induced built-in electric fields boost electrochemical nitrate reduction to ammonia over CuO@MnO₂ core-shell hierarchical nanoarrays, *J. Mater. Chem. A*, 2022, **10**, 16883–16890.

17 T. Ren, Z. Yu, H. Yu, K. Deng, Z. Wang, X. Li, H. Wang, L. Wang and Y. Xu, Interfacial polarization in metal-organic framework reconstructed Cu/Pd/CuO_x multi-phase heterostructures for electrocatalytic nitrate reduction to ammonia, *Appl. Catal., B*, 2022, **318**, 121805.

18 Y. Zhang, X. Chen, W. Wang, L. Yin and J. C. Crittenden, Electrocatalytic nitrate reduction to ammonia on defective Au₁Cu (111) single-atom alloys, *Appl. Catal., B*, 2022, **310**, 121346.

19 X. Li, S. Wang, G. Wang, P. Shen, D. Ma and K. Chu, Mo₂C for electrocatalytic nitrate reduction to ammonia, *Dalton Trans.*, 2022, **51**, 17547–17552.

20 S. Zhang, M. Li, J. Li, Q. Song and X. Liu, High-ammonia selective metal-organic framework-derived Co-doped Fe/Fe₂O₃ catalysts for electrochemical nitrate reduction, *Proc. Natl. Acad. Sci.*, 2022, **119**, e2115504119.

21 W. J. Sun, H. Q. Ji, L. X. Li, H. Y. Zhang, Z. K. Wang, J. H. He and J. M. Lu, Built-in electric field triggered interfacial accumulation effect for efficient nitrate removal at ultra-low concentration and electroreduction to ammonia, *Angew. Chem., Int. Ed.*, 2021, **60**, 22933–22939.

22 L. Li, C. Tang, X. Cui, Y. Zheng, X. Wang, H. Xu, S. Zhang, T. Shao, K. Davey and S. Z. Qiao, Efficient nitrogen fixation to ammonia through integration of plasma oxidation with electrocatalytic reduction, *Angew. Chem.*, 2021, **133**, 14250–14256.

23 P. Gao, Z. H. Xue, S. N. Zhang, D. Xu, G. Y. Zhai, Q. Y. Li, J. S. Chen and X. H. Li, Schottky barrier-induced surface electric field boosts universal reduction of NO_x[–] in water to ammonia, *Angew. Chem.*, 2021, **133**, 20879–20884.

24 P. Li, Z. Jin, Z. Fang and G. Yu, A single-site iron catalyst with preoccupied active centers that achieves selective ammonia electrosynthesis from nitrate, *Energy Environ. Sci.*, 2021, **14**, 3522–3531.

25 Y. Guo, R. Zhang, S. Zhang, Y. Zhao, Q. Yang, Z. Huang, B. Dong and C. Zhi, Pd doping-weakened intermediate adsorption to promote electrocatalytic nitrate reduction on TiO₂ nanoarrays for ammonia production and energy supply with zinc–nitrate batteries, *Energy Environ. Sci.*, 2021, **14**, 3938–3944.

26 J. Zhang, T. Wang, D. Pohl, B. Rellinghaus, R. Dong, S. Liu, X. Zhuang and X. Feng, Interface engineering of MoS₂/Ni₃S₂ heterostructures for highly enhanced electrochemical

overall-water-splitting activity, *Angew. Chem., Int. Ed.*, 2016, **55**, 6702–6707.

27 H. Li, C. Tsai, A. L. Koh, L. Cai, A. W. Contryman, A. H. Fragapane, J. Zhao, H. S. Han, H. C. Manoharan, F. Abild-Pedersen, J. K. Nørskov and X. Zheng, Activating and optimizing MoS_2 basal planes for hydrogen evolution through the formation of strained sulphur vacancies, *Nat. Mater.*, 2016, **15**, 48–53.

28 Q. Xiang, J. Yu and M. Jaroniec, Synergetic effect of MoS_2 and graphene as cocatalysts for enhanced photocatalytic H_2 production activity of TiO_2 nanoparticles, *J. Am. Chem. Soc.*, 2012, **134**, 6575–6578.

29 Q. Li, Y. Guo, Y. Tian, W. Liu and K. Chu, Activating VS_2 basal planes for enhanced NRR electrocatalysis: the synergistic role of S-vacancies and B dopants, *J. Mater. Chem. A*, 2020, **8**, 16195–16202.

30 J. Zhang, C. Zhang, Z. Wang, J. Zhu, Z. Wen, X. Zhao, X. Zhang, J. Xu and Z. Lu, Synergistic interlayer and defect engineering in VS_2 nanosheets toward efficient electrocatalytic hydrogen evolution reaction, *Small*, 2018, **14**, 1703098.

31 K. Chu, Y. Liu, Y. Li, Y. Guo, Y. Tian and H. Zhang, Multi-functional Mo-doping in MnO_2 nanoflowers toward efficient and robust electrocatalytic nitrogen fixation, *Appl. Catal., B*, 2020, **264**, 118525.

32 N. Liu, D. Cao, W. Liu, H. Zhang, Y. Zhu, L. Chang, D. Wu and D. Cheng, Constructing La-doped ultrathin Co-based nanostructured electrocatalysts for high-performance water oxidation process, *Int. J. Hydrogen Energy*, 2022, **47**, 14504–14514.

33 X. Yang, Y. Ma, Y. Liu, K. Wang, Y. Wang, M. Liu, X. Qiu, W. Li and J. Li, Defect-induced Ce-doped Bi_2WO_6 for efficient electrocatalytic N_2 reduction, *ACS Appl. Mater. Interfaces*, 2021, **13**, 19864–19872.

34 Y. Luo, K. Chen, G. Wang, G. Zhang, N. Zhang and K. Chu, Ce-doped MoS_{2-x} nanoflower arrays for electrocatalytic nitrate reduction to ammonia, *Inorg. Chem. Front.*, 2023, DOI: [10.1039/d2qi01798a](https://doi.org/10.1039/d2qi01798a).

35 P. Shen, G. Wang, K. Chen, J. Kang, D. Ma and K. Chu, Selenium-vacancy-rich WSe_2 for nitrate electroreduction to ammonia, *J. Colloid Interface Sci.*, 2023, **629**, 563–570.

36 P. Shen, X. Li, Y. Luo, Y. Guo, X. Zhao and K. Chu, High-efficiency N_2 electroreduction enabled by Se-vacancy-rich WSe_{2-x} in water-in-salt electrolytes, *ACS Nano*, 2022, **16**, 7915–7925.

37 X. Li, G. Zhang, P. Shen, X. Zhao and K. Chu, A defect engineered p-block SnS_{2-x} catalyst for efficient electrocatalytic NO reduction to NH_3 , *Inorg. Chem. Front.*, 2023, **10**, 280–287.

38 Y. Luo, P. Shen, X. Li, Y. Guo and K. Chu, Sulfur-deficient $\text{Bi}_2\text{S}_{3-x}$ synergistically coupling $\text{Ti}_3\text{C}_2\text{T}_x$ -MXene for boosting electrocatalytic N_2 reduction, *Nano Res.*, 2022, **15**, 3991–3999.

39 Y. Luo, Q. Li, Y. Tian, Y. Liu and K. Chu, Amorphization engineered VSe_{2-x} nanosheets with abundant Se-vacancies for enhanced N_2 electroreduction, *J. Mater. Chem. A*, 2022, **10**, 1742–1749.

40 L. Zhang, M. Zhou, A. Wang and T. Zhang, Selective hydrogenation over supported metal catalysts: from nanoparticles to single atoms, *Chem. Rev.*, 2019, **120**, 683–733.

41 K. Chen, Y. Zhang, J. Xiang, X. Zhao, X. Li and K. Chu, p-block antimony single-atom catalysts for nitric oxide electroreduction to ammonia, *ACS Energy Lett.*, 2023, **8**, 1281–1288.

42 K. Chen, G. Zhang, X. Li, X. Zhao and K. Chu, Electrochemical NO reduction to NH_3 on Cu single atom catalyst, *Nano Res.*, 2023, DOI: [10.1007/s12274-023-5384-9](https://doi.org/10.1007/s12274-023-5384-9).

43 K. Chen, J. Wang, J. Kang, X. Lu, X. Zhao and K. Chu, Atomically Fe-doped MoS_{2-x} with Fe-Mo dual sites for efficient electrocatalytic NO reduction to NH_3 , *Appl. Catal., B*, 2023, **324**, 122241.

44 K. Chu, J. Wang, Y. Liu, Q. Li and Y. Guo, Mo-doped SnS_2 with rich S-vacancies for highly efficient electrocatalytic N_2 reduction: the critical role of Mo-Sn-Sn trimer, *J. Mater. Chem. A*, 2020, **8**, 7117–7124.

45 X. Li, K. Chen, X. Lu, D. Ma and K. Chu, Atomically dispersed Co catalyst for electrocatalytic NO reduction to NH_3 , *Chem. Eng. J.*, 2023, **454**, 140333.

46 X. Li, P. Shen, Y. Luo, Y. Li, Y. Guo, H. Zhang and K. Chu, PdFe single-atom alloy metallene for N_2 electroreduction, *Angew. Chem.*, 2022, **134**, e202205923.

47 P. Shen, X. Li, Y. Luo, N. Zhang, X. Zhao and K. Chu, Ultra-efficient N_2 electroreduction achieved over a rhodium single-atom catalyst (Rh_1/MnO_2) in water-in-salt electrolyte, *Appl. Catal., B*, 2022, **316**, 121651.

48 K. Chen, J. Wang, H. Zhang, D. Ma and K. Chu, Self-tandem electrocatalytic NO reduction to NH_3 on W single atom catalyst, *Nano. Lett.*, 2023, DOI: [10.1021/acs.nanolett.2c04444](https://doi.org/10.1021/acs.nanolett.2c04444).

49 W. Zhang, M. Jiang, S. Yang, Y. Hu, B. Mu, Z. Tie and Z. Jin, *In situ* grown CuO_x nanowire forest on copper foam: A 3D hierarchical and freestanding electrocatalyst with enhanced carbonaceous product selectivity in CO_2 reduction, *Nano Res. Energy*, 2022, **1**, e9120033.

50 L. Zhang, J. Liang, L. Yue, K. Dong, J. Li, D. Zhao, Z. Li, S. Sun, Y. Luo, Q. Liu, G. Cui, A. Ali Alshehri, X. Guo and X. Sun, Benzoate anions-intercalated NiFe-layered double hydroxide nanosheet array with enhanced stability for electrochemical seawater oxidation, *Nano Res. Energy*, 2022, **1**, e9120028.

51 F. Guo, M. Zhang, S. Yi, X. Li, R. Xin, M. Yang, B. Liu, H. Chen, H. Li and Y. Liu, Metal-coordinated porous poly-dopamine nanospheres derived $\text{Fe}_3\text{N}-\text{FeCo}$ encapsulated N-doped carbon as a highly efficient electrocatalyst for oxygen reduction reaction, *Nano Res. Energy*, 2022, **1**, e9120027.

52 X. Li, P. Shen, X. Li, D. Ma and K. Chu, Sub-nm RuO_x clusters on Pd metallene for synergistically enhanced nitrate electroreduction to ammonia, *ACS Nano*, 2023, **17**, 1081–1090.

53 K. Chen, Z. Ma, X. Li, J. Kang, D. Ma and K. Chu, Single-atom Bi alloyed Pd metallene for nitrate electroreduction to ammonia, *Adv. Funct. Mater.*, 2023, DOI: [10.1002/adfm.202209890](https://doi.org/10.1002/adfm.202209890).

54 G. Wang, P. Shen, Y. Luo, X. Li, X. Li and K. Chu, A vacancy engineered MnO_{2-x} electrocatalyst promotes electroreduction of nitrate to ammonia, *Dalton Trans.*, 2022, **51**, 9206–9212.

55 G. Zhang, X. Li, K. Chen, Y. Guo, D. Ma and K. Chu, Tandem electrocatalytic nitrate reduction to ammonia on MBenes, *Angew. Chem., Int. Ed.*, 2023, DOI: [10.1002/anie.202300054](https://doi.org/10.1002/anie.202300054).

56 N. Zhang, G. Zhang, P. Shen, H. Zhang, D. Ma and K. Chu, Lewis acid Fe-V pairs promote nitrate electroreduction to ammonia, *Adv. Funct. Mater.*, 2023, DOI: [10.1002/adfm.202211537](https://doi.org/10.1002/adfm.202211537).

57 Y. Luo, K. Chen, P. Shen, X. Li, X. Li, Y. Li and K. Chu, B-doped MoS_2 for nitrate electroreduction to ammonia, *J. Colloid Interface Sci.*, 2023, **629**, 950–957.

58 K. Chu, X. Li, Q. Li, Y. Guo and H. Zhang, Synergistic enhancement of electrocatalytic nitrogen reduction over boron nitride quantum dots decorated Nb_2CT_x -MXene, *Small*, 2021, **17**, 2102363.

59 Y. Cheng, X. Li, P. Shen, Y. Guo and K. Chu, MXene quantum dots/copper heterostructure for synergistically enhanced N_2 electroreduction, *Energy Environ. Mater.*, 2023, **6**, e12268.

60 Q. Li, P. Shen, Y. Tian, X. Li and K. Chu, Metal-free BN quantum dots/graphitic C_3N_4 heterostructure for nitrogen reduction reaction, *J. Colloid Interface Sci.*, 2022, **606**, 204–212.

61 K. Chu, Y. Luo, P. Shen, X. Li, Q. Li and Y. Guo, Unveiling the synergy of O-vacancy and heterostructure over MoO_{3-x} -MXene for N_2 electroreduction to NH_3 , *Adv. Energy Mater.*, 2022, **12**, 2103022.

62 X. Li, Y. Luo, Q. Li, Y. Guo and K. Chu, Constructing an electron-rich interface over an Sb/ Nb_2CT_x -MXene heterojunction for enhanced electrocatalytic nitrogen reduction, *J. Mater. Chem. A*, 2021, **9**, 15955–15962.

63 K. Chen, G. Wang, Y. Guo, D. Ma and K. Chu, Iridium single-atom catalyst for highly efficient NO electroreduction to NH_3 , *Nano Res.*, 2023, DOI: [10.1007/s12274-023-5556-7](https://doi.org/10.1007/s12274-023-5556-7).

64 D. Wu, P. Lv, J. Wu, B. He, X. Li, K. Chu, Y. Jia and D. Ma, Catalytic active centers beyond transition metals: atomically dispersed alkaline-earth metals for electroreduction of nitrate to ammonia, *J. Mater. Chem. A*, 2023, **11**, 1817–1828.

65 B. He, P. Lv, D. Wu, X. Li, R. Zhu, K. Chu, D. Ma and Y. Jia, Confinement catalysis of a single atomic vacancy assisted by aliovalent ion doping enabled efficient NO electroreduction to NH_3 , *J. Mater. Chem. A*, 2022, **10**, 18690–18700.

66 Y. Wang, A. Xu, Z. Wang, L. Huang, J. Li, F. Li, J. Wicks, M. Luo, D.-H. Nam, C.-S. Tan, Y. Ding, J. Wu, Y. Lum, C.-T. Dinh, D. Sinton, G. Zheng and E. H. Sargent, Enhanced nitrate-to-ammonia activity on copper-nickel alloys via tuning of intermediate adsorption, *J. Am. Chem. Soc.*, 2020, **142**, 5702–5708.